Fuel 405 (2026) 136782

Contents lists available at ScienceDirect

Fuel

journal homepage: www.elsevier.com/locate/fuel

Full Length Article

Fe-Ce interaction-driven active site modulation in a porous MOF for oxygen evolution reaction

Sheraz Muhammad [a], Lixia Wang [a], Mingcheng Gao [b], Sumayya Khan [a], Wentao Xu [a], Asif Ali [c], Tayirjan Taylor Isimjan [d,*], Shohreh Azizi [e], Xiulin Yang [a,*]

[a] Guangxi Key Laboratory of Low Carbon Energy Materials, School of Chemistry and Pharmaceutical Sciences, Guangxi Normal University, Guilin 541004, China
[b] School of Chemistry, Fuzhou University, Fuzhou, China
[c] Department of Applied Chemistry, Graduate School of Science and Engineering, Doshisha University, Kyoto, Japan
[d] Saudi Arabia Basic Industries Corporation (SABIC) at King Abdullah University of Science and Technology (KAUST), Thuwal 23955-6900, Saudi Arabia
[e] UNESCO-UNISA Africa Chair in Nanosciences/Nanotechnology, College of Graduate Studies, University of South Africa, Muckleneuk Ridge, Pretoria 0181, South Africa

A R T I C L E I N F O

Keywords:
Metal-organic frameworks
Operando spectroscopy
Oxygen evolution reaction
Adsorbate evolution mechanism
Overall water splitting

A B S T R A C T

Developing efficient and stable noble-metal-free electrocatalysts for the oxygen evolution reaction (OER) is crucial for advancing renewable energy technologies. Herein, we synthesized $Fe_{1.5}$Ce-NDC through a solvothermal approach, which exhibited a hierarchically porous morphology that maximize active site exposure and facilitates rapid mass transport. Synergistic Fe-Ce interactions optimize electronic structure, accelerate charge transfer through dynamic surface reconstruction, and form highly active FeOOH species that ensure long-term catalytic stability. Thus, $Fe_{1.5}$Ce-NDC achieves an ultra-low overpotential of 236 mV at 10 mA cm^{-2} and Tafel slope of 52 mV dec^{-1}, significantly outperforming conventional RuO_2 catalysts, even though maintaining exceptional stability for 76 h at 100 mA cm^{-2}. *Operando* Raman and ATR-FTIR spectroscopy confirm that $Fe_{1.5}$Ce-NDC follows an adsorbate evolution mechanism (AEM), where Ce facilitates Fe stabilization and enhances reaction kinetics. Furthermore, in two-electrode system $Fe_{1.5}$Ce-NDC$^{(+)}$ || Pt/C$^{(-)}$ achieves low cell voltage of 1.65 V at 100 mA cm^{-2} and maintains stability over 100 h at 100 mA cm^{-2}, demonstrating durability under practical conditions. These results underscore transformative nature of Fe-Ce interactions in optimizing charge transfer, stabilizing active sites, and enhancing OER efficiency, establishing Fe-based MOFs as remarkably effective, durable, and scalable catalyst for sustainable energy conversion and hydrogen production applications.

1. Introduction

In recent years, electrochemical water splitting has gained attention as a promising approach for efficient and clean hydrogen production, involving two key half-reactions anodic OER and cathodic hydrogen evolution reaction (HER). The OER is the rate-determining step for effective water electrolysis [1]. Nevertheless, because of the intrinsic kinetic limitations of the OER, a significant overpotential is often necessary to attain a high catalytic current density [2]. Hence, an effective electrocatalyst is crucial to enhance the OER rate. While precious metals like Ru and Ir demonstrate exceptional OER performance and stability in alkaline condition, their limited availability and elevated expense hinder broad adoption in catalytic applications [3,4]. In light of this, further exploring low-cost, high-performance electrocatalysts is essential for enhancing OER efficiency and improving the economic viability of this energy conversion process.

MOFs representing an emerging class of porous crystalline substances made up of metallic nodes and carbon-based linker. Owing to their high surface area, varied architectures, accessible pore networks, and tunable active site arrangements make them highly promising for OER electrocatalysis [5–8]. Among them, Ce-MOFs have drawn considerable attention owing to their distinctive properties, such as the ability to facilitate strong interactions between cerium ions and other catalytic sites [9]. These features enable Ce-MOFs to be highly effective in various electrocatalytic reactions, including oxygen and hydrogen evolution. Ceria (CeO_2), an important lanthanide-based compound, features multiple valence states of Ce^{3+} and Ce^{4+}, allowing for dynamic surface oxygen exchange and efficient electronic conductivity [10]. This

* Corresponding authors.
E-mail addresses: isimjant@cabic.com (T.T. Isimjan), xlyang@gxnu.edu.cn (X. Yang).

https://doi.org/10.1016/j.fuel.2025.136782
Received 28 July 2025; Received in revised form 1 September 2025; Accepted 5 September 2025
Available online 10 September 2025

makes it a suitable platform for enhanced electron coupling in combination with other advanced materials. While CeO_2 on its own is not catalytically active, its ability to transition between Ce^{3+} and Ce^{4+} has recently been utilized as an OER promoter, driving the advancement of efficient electrocatalytic systems [11].

Introducing another metal is a promising approach to tailor the electronic structure of MOFs, enabling improved charge transfer during the OER, create favorable sites for intermediate adsorption and release, and improve catalytic efficiency. Additionally, second can modify the electronic configuration and band gap to fine-tune the binding energy of intermediates, thus accelerating the oxygen evolution [12]. For instance, *Liao et al.,* prepared Co-MOF doped with cerium on carbon substrate (CoCe-MOF/CP), achieving excellent catalytic performance with a minimal overpotential and excellent durability. The study showed that Ce-doping optimized the electronic configuration of cobalt sites, enhancing OER performance [13]. Additionally, *Zhao et al.* developed ultrathin nickel–iron MOF nanosheets. Their ultrathin structure, hydrophilicity, and Ni/Fe bimetallic synergy result in high OER activity and stability. The study exhibited that Fe doping enhanced the OER activity through optimizing the reaction rate as well as lowering energy barrier [14]. Furthermore, *Dai et al.,* developed a Fe-doped Co-MOF, where iron doping as well as amorphous interfaces enhance electron transfer, expose more active sites, and optimize the electronic configuration of the cobalt active center, resulting in excellent OER performance and remarkable stability [15]. Introducing Fe into the Ce-NDC framework can enhance its electronic structure, redox activity, and catalytic performance. As a transition metal, Fe forms Fe-O bonds that promote faster electron transfer, improved charge transport, and better adsorption of oxygen intermediates, which are key to efficient OER. The synergy between Ce and Fe combines Ce redox stability with Fe surface reactivity, creating new active sites and boosting catalytic efficiency. However, FeCe-NDC has not yet been reported, and we are exploring it for the first time as a potential enhancement for catalytic performance in OER catalysis.

Herein, we fabricated $Fe_{1.5}$Ce-NDC through solvothermal approach, exhibiting superior electrocatalytic OER activity. The $Fe_{1.5}$Ce-NDC catalyst demonstrated exceptional OER performance, achieving low overpotentials of 236 mV at 10 mA cm^{-2} and 305 mV at 100 mA cm^{-2}. It showed excellent durability of 76 h at 100 mA cm^{-2}. Dynamic surface reconstruction during OER was observed by *operando* Raman and ATR-FTIR analysis, wherein $Fe_{1.5}$Ce-NDC transformed into FeOOH, the actual active species, thereby facilitating efficient charge transfer and sustained catalytic activity. Furthermore, the two-electrode electrolyzer system $Fe_{1.5}$Ce-NDC$^{(+)}$ || Pt/C$^{(-)}$ exhibited an impressive performance of 1.65 V at 100 mA cm^{-2}, and maintained robust stability for 100 h. Synergy of Fe, combined with Ce and carbon-rich framework, effectively optimized electronic interactions, enhanced the stability of active sites, and significantly improved OER activity and durability.

2. Experimental section

2.1. Chemical reagents

Ruthenium chloride ($RuCl_3$), commercial Pt/C (20 wt% Pt), cerium (III) nitrate hydrate ($Ce(NO_3)_3 \cdot 6H2O$, 99 %), and iron (II) nitrate non-ahydrate ($Fe(NO_3)_3 \cdot 9H_2O$, ≥98 %) were obtained from Inno-chem. Sulfuric acid (H_2SO_4, 98.0 %), potassium hydroxide (KOH, 98.0 %), absolute ethanol (C_2H_5OH, ≥99 %), 2,6-naphthalenedicarboxylic acid (NDC, ≥99 %), N,N-dimethylformamide (DMF, ≥99 %), Nafion solution (5 wt%), and nickel foam (NF) were bought from Xilong Science Co., Ltd. NF with width of 1.6 mm, was cut into pieces of 1.5 cm × 3 cm. All the chemicals used were of high purity suitable for analysis and were employed as received without additional purification steps.

2.2. Fabrication of Ce-NDC

The fabrication of Ce-NDC was carried out by dissolving 1 mM of Ce $(NO_3)_3 \cdot 6H_2O$ and 1.5 mM of NDC in a solution of 30 mL DMF, 5 mL ethanol, and 5 mL water. The solution was sonicated for 20 min to ensure complete dissolution of the reagents. Pre-treated NF, which had been cleaned in 0.5 M H_2SO_4, ethanol, and deionized water for 10 min each, was immersed in the prepared solution. The solution was then placed into a Teflon-lined stainless-steel autoclave, sealed, and heated at 120 °C for 10 h. After cooling to room temperature, the sample was thoroughly washed multiple times with ethanol and dried overnight at 60 °C, yielding the Ce-NDC/NF electrocatalyst with a mass loading of 2.4 mg cm^{-2}.

2.3. Fabrication of Fe_xCe-NDC

The fabrication of Fe_xCe-NDC was carried out using the same method as for Ce-NDC, with the addition of varying amounts of $Fe(NO_3)_3 \cdot 9H_2O$ (X = 0.5, 1, 1.5, and 2 mM) to 1 mM $Ce(NO_3)_3 \cdot 6H_2O$ and 1.5 mM NDC in a mixture of 30 mL DMF, 5 mL ethanol, and 5 mL water. The solution was sonicated for 20 min to ensure complete dissolution of the reagents. Pre-treated NF, was immersed in the prepared solution. The solution was then placed into a Teflon-lined stainless-steel autoclave, sealed, and heated at 120 °C for 10 h. After cooling to room temperature, the sample was washed with ethanol and dried overnight at 60 °C, yielding the Fe_xCe-NDC/NF electrocatalyst with mass loading of 2.1, 1.8, 2.9 and 3.1 mg cm^{-2}.

2.4. Fabrication of RuO_2 and Pt/C electrodes

$RuCl_3$ was milled in a mortar until a fine, homogeneous powder was obtained, next calcined in air at 400 °C for 3 h to produce RuO_2. To prepare the electrode materials, 2.1 mg of commercial Pt/C powder or 3 mg of RuO_2 was dispersed in a solution of 230 μL deionized water, 230 μL C_2H_5OH, and 5 μL of 5 wt% Nafion. The resulting suspension was subjected to ultrasonication for 30 min to ensure complete dispersion. After sonication, 230 μL of this ink was drop-cast onto a 1 cm × 1 cm piece of NF and allowed to air-dry at room temperature.

3. Results and discussion

3.1. Synthesis and characterization

$Fe_{1.5}$Ce-NDC was grown directly onto NF through solvothermal approach (Fig. 1a). Cleaned NF was placed in a Teflon-lined autoclave containing a solution of NDC, $Ce(NO_3)_3 \cdot 6H_2O$, and $Fe(NO_3)_3 \cdot 9H_2O$, then heated at 120 °C for 10 h. Once cooled, the foam was lifted out and dried at 60 °C overnight. The strong X-ray diffraction (XRD) signals from its $Fe_{1.5}$Ce-NDC layer obscured any minor phases. To overcome this, the precipitate that had settled in the reactors bottom were collected by centrifugation, dried at 60 °C overnight, and used for subsequent XRD analysis.

The coordination environment of the metal ions within the framework plays a crucial role in its structural stability and connectivity. The structural unit of the MOF consists of the Ce and Fe metal ions, which are coordinated to the oxygen atoms of the carboxylate groups in NDC ligands. Ce, with its larger ionic radius, forms a more flexible coordination environment. At the same time, Fe is coordinated to the oxygen atoms of the carboxylate groups, forming Fe-O bonds with a preferred octahedral geometry [16]. Additionally, Fe forms bridging interactions between NDC molecules, linking the Fe centers. The Fe-O-Ce bridging interactions, where both metals coordinate to the same oxygen atoms of the carboxylate groups, create a stable bimetallic framework. These structural units throughout the framework, significantly enhance the structural integrity and connectivity of the MOF (**Fig. S1**). The structural analysis of the catalysts was conducted using XRD. The pristine Ce-NDC

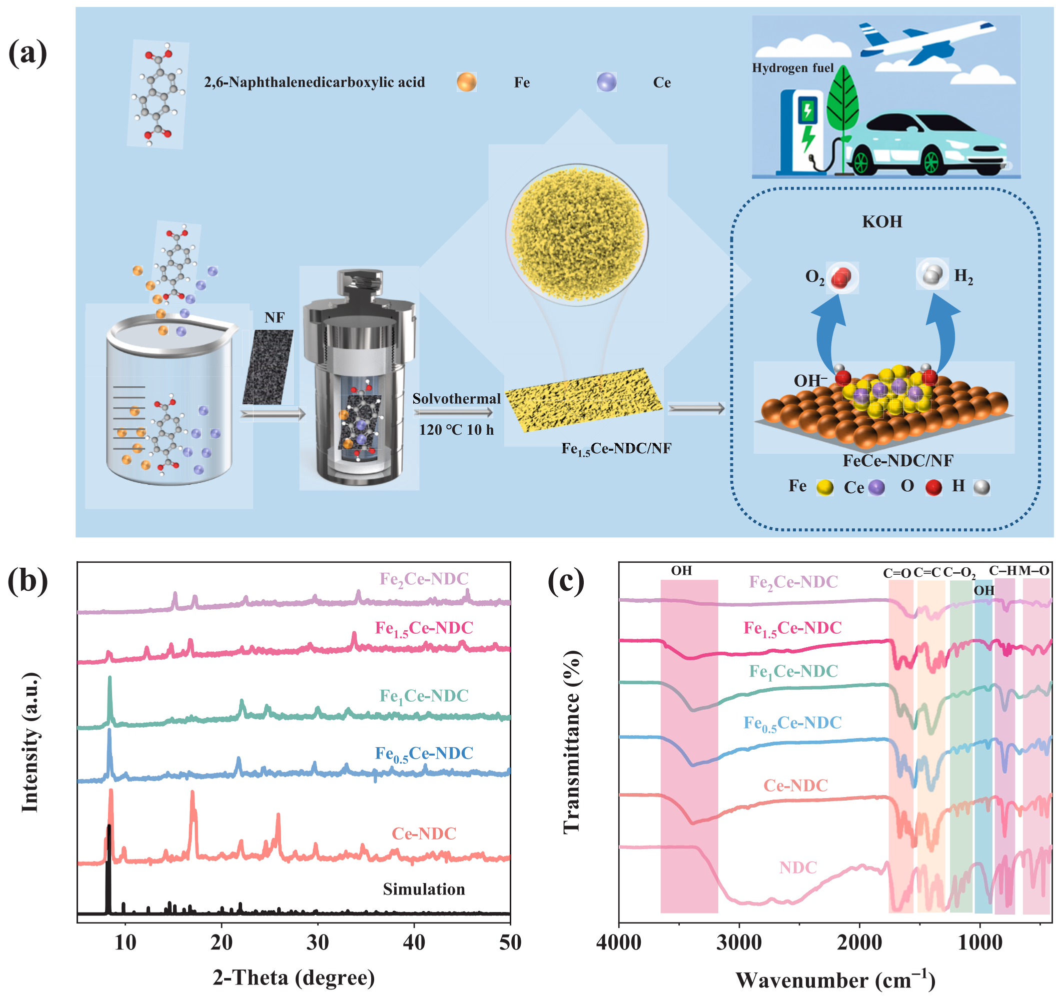

Fig. 1. (a) Scheme of the preparation method and the OER mechanism on the FeCe-NDC/NF surface. (b) XRD patterns of Ce-NDC and Fe_xCe-NDC, along with simulated data from the Ce-NDC crystal structure. (c) FTIR spectra of NDC, Ce-NDC, and Fe_xCe-NDC.

exhibits characteristic diffraction peaks at approximately 8.52°, which align well with theoretical simulations of the Ce-NDC structure, as described in the crystallographic information file (CIF, Cambridge Crystallographic Data Centre No. 989479) [17]. $Fe_{0.5}$Ce-NDC, Fe_1Ce-NDC and $Fe_{1.5}$Ce-NDC retained a similar crystal structure to Ce-NDC, indicating that the introduction of Fe without significant alteration to the overall framework (Fig. 1b). Notably, the diffraction peak intensity diminishes with increasing Fe concentration, signifying successful Fe incorporation into the Ce-NDC. In Fe_2Ce-NDC, the diffraction peaks are almost entirely attenuated, indicating significant structural disruption of the Ce-NDC due to high Fe concentration, as verified by SEM. These findings highlight the effect of diverse concentrations of Fe on the crystallinity and its structural integrity of the Ce-NDC. The Fourier transform infrared (FTIR) spectrum of synthesized catalysts reveals several key functional groups (Fig. 1c). The extended broad peaks at 3000–3400 cm^{-1} indicate the occurrence of hydroxyl. The C=O stretching vibration around 1674 cm^{-1} and C=C stretching at 1400–1500 cm^{-1} suggest the presence of carbonyl and conjugated C–C bonds from the NDC ligand, which contribute to the structural stability of the framework [18]. Additionally, the C-O_2 stretch around 1200 cm^{-1} shows the existence of carboxylate groups, while the second OH stretch below 918 cm^{-1} reflects hydroxyl groups involved in metal–oxygen interactions [19]. The C–H and metal–oxygen (M–O) stretching below 1000 cm^{-1} further emphasizes Ce-O and Fe-O bonding, affirming the incorporation of Ce and Fe into the structure.

For surface morphology and microstructure analysis, scanning electron microscopy (SEM) was used to examine the various synthesized materials [20,21]. Figs. 2**a-b** show the hierarchically porous, nanosheet-based morphology of Ce-NDC and $Fe_{1.5}$Ce-NDC, with a nanostructured or clustered and aggregated appearance. Similarly, $Fe_{0.5}$Ce-NDC and Fe_1Ce-NDC exhibit similar morphologies (**Figs. S2a-b**). In contrast, Fe_2Ce-NDC presents a more uniform and nanosheet-based morphology (**Fig. S2c**). The SEM images of Ce-NDC and the various Fe_xCe-NDC catalysts reveal noticeable changes in the morphology as the concentration of Fe increases. Specifically, as Fe concentration increases, the morphology shifts from hierarchically porous, nanosheet to more organized structures. These findings indicate that the Fe concentration is pivotal in influencing the morphology. Higher Fe content facilitates the formation of more uniform less porous structures, especially in Fe_2Ce-NDC.

The transmission electron microscopy (TEM) image reveals that $Fe_{1.5}$Ce-NDC exhibits a flower-like, nanosheet-based architecture with loosely stacked layers and abundant porosity, indicative of high-surface area and numerous exposed active sites (Fig. 2c). High-resolution transmission electron microscopy (HR-TEM) image of $Fe_{1.5}$Ce-NDC exhibits indistinct lattice fringes, attributed to localized structural defects and its electron beam irradiation sensitivity (Fig. 2d). MOFs are highly susceptible to damage under HR-TEM conditions [22–24]. Furthermore, selected area electron diffraction (SAED) patterns of $Fe_{1.5}$Ce-NDC displays diffuse rings, indicating a partially or low crystalline structure (Fig. 2e). This observation and the hierarchically porous morphology seen in SEM, suggests that $Fe_{1.5}$Ce-NDC exhibits a partially crystalline

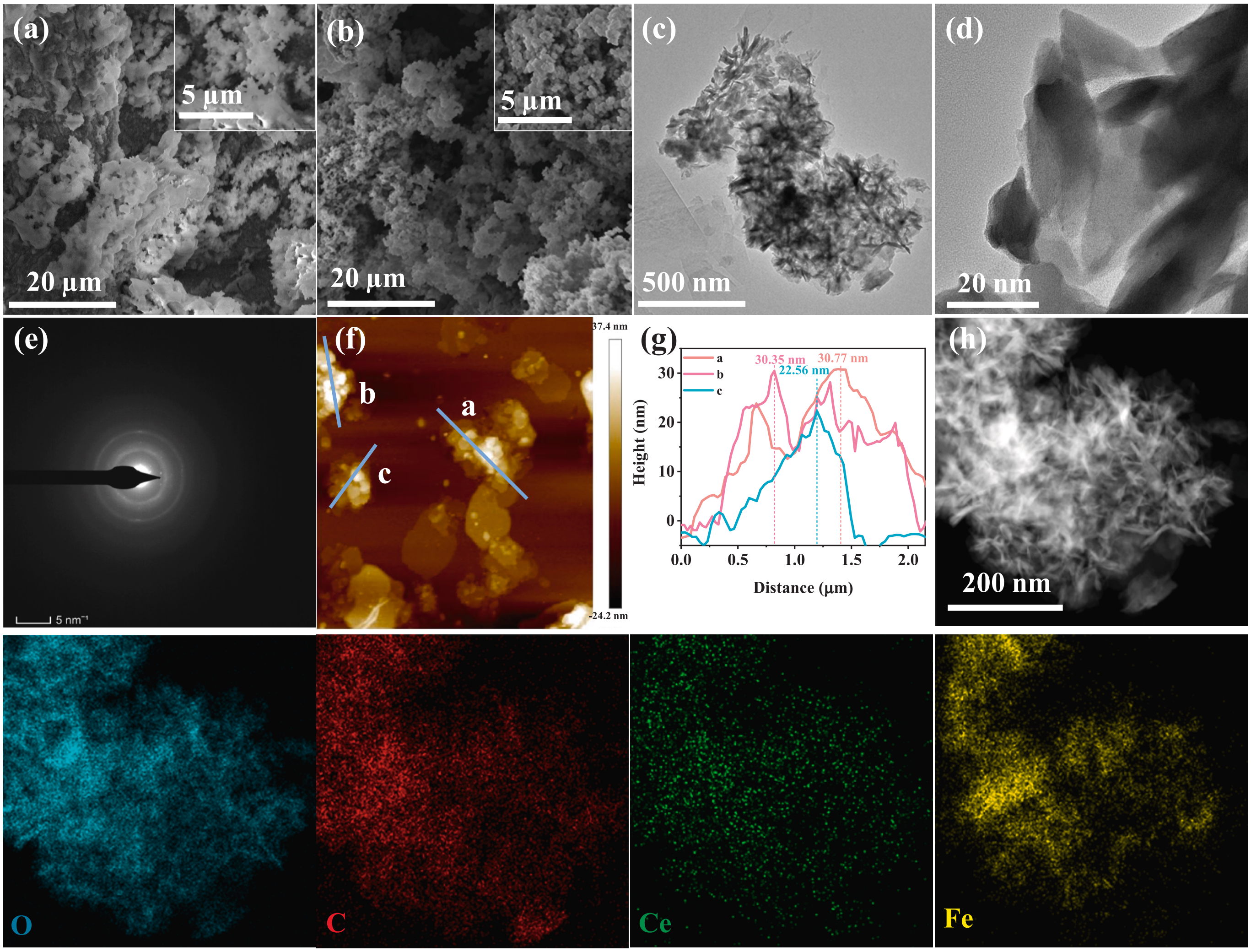

Fig. 2. SEM images of (a) Ce-NDC and (b) $Fe_{1.5}$Ce-NDC. (c) TEM, (d) HR-TEM, (e) SAED pattern, (f) AFM, (g) corresponding height profiles, (h) HAADF-STEM and elemental mapping images of $Fe_{1.5}$Ce-NDC.

framework with localized structural disorder characteristics commonly found in MOF-based materials [25]. The diffuse nature of the rings further aligns with the observation that the $Fe_{1.5}$Ce-NDC structure is sensitive to electron beam irradiation, which can lead to structural degradation and localized disorder, as seen in the HR-TEM results. The atomic force microscopy (AFM) image shows the surface morphology, showing distinct features with height variations (Fig. 2f). The corresponding height profiles indicate an average thickness of about 27.89 nm of $Fe_{1.5}$Ce-NDC (Fig. 2g), highlighting the nanometer-scale surface roughness that contributes to the materials high surface area for catalytic reactions. Additionally, high-angle annular dark field scanning transmission electron microscopy (HAADF-STEM) further confirms the flower-like, porous nanosheet architecture of $Fe_{1.5}$Ce-NDC. At the same time, elemental mapping reveals that O, Ce, Fe, and C are homogeneously dispersed throughout the structure (Fig. 2h) [26,27]. The energy dispersive X-ray spectroscopy (EDS) spectra, confirms the fruitful preparation, structural integrity, and high purity of the $Fe_{1.5}$Ce-NDC catalyst. Prominent peaks for C and O correspond to the organic ligand framework, while distinct peaks for Fe and Ce validate their incorporation into the MOF structure (**Fig. S3**).

The thermogravimetric analysis (TGA) and derivative thermogravimetry (DTG) of Ce-NDC and $Fe_{1.5}$Ce-NDC show distinct thermal behaviors. For Ce-NDC, the first weight loss of 2.59 % occurs at 113 °C, ascribed to the removal of adsorbed moisture, after that 10.7 % loss at 251 °C, indicating the decomposition of the NDC ligand. A further loss of 2.57 % is observed at 275 °C, and the significant weight loss of 42.87 % occurs around 377 °C, corresponding to the breakdown of the organic linker (Fig. 3a) [28]. In contrast, $Fe_{1.5}$Ce-NDC exhibits a smaller initial weight loss of 1.99 % at 167 °C, reflecting lower moisture retention [29]. The experiences additional weight losses of 5.03 % at 277 °C, 7.07 % at 354 °C, and 22.16 % at 422 °C, with the latter corresponding to the decomposition of the organic linker (Fig. 3b) [14]. The $Fe_{1.5}$Ce-NDC demonstrates higher thermal robustness compared to Ce-NDC, with a more stable residual mass. The improved thermal stability of $Fe_{1.5}$Ce-NDC may enhance its suitability for OER electrocatalysis, as higher thermal stability helps maintain phase integrity and catalytic activity under operating conditions [30].

High resolution X-ray photoelectron spectroscopy (XPS) was used to examine the valence states and elemental arrangement of Ce-NDC and $Fe_{1.5}$Ce-NDC materials. The XPS survey spectrum (Fig. 3c) confirmed the presence of C, O, Ce, and Fe, which aligns with the findings from the EDS analysis. The C 1 s spectra was deconvoluted into 3 different peaks, assigned to C=C/C–C, C-O and C=O at 284.59, 285.51, and 288.3 eV, respectively (**Fig. S4**) [22,31,32]. As depicted in Fig. 3d, the O 1 s XPS spectra displays peaks, assigned to metal-O, O-C=O, and H_2O_{ads} at 529.88, 531.11, and 532.17 eV [33]. The Ce 3d XPS spectra of Ce-NDC and $Fe_{1.5}$Ce-NDC exhibit four characteristic spin–orbit doublets, with prominent peaks at 881.10 (1) and 885.05 eV (2) in $3d_{5/2}$ region, which are assigned to Ce^{3+}, confirming the dominant trivalent cerium configuration. Peaks at 889.09 (3) and 894.14 eV (4), assigned to Ce^{4+}, are

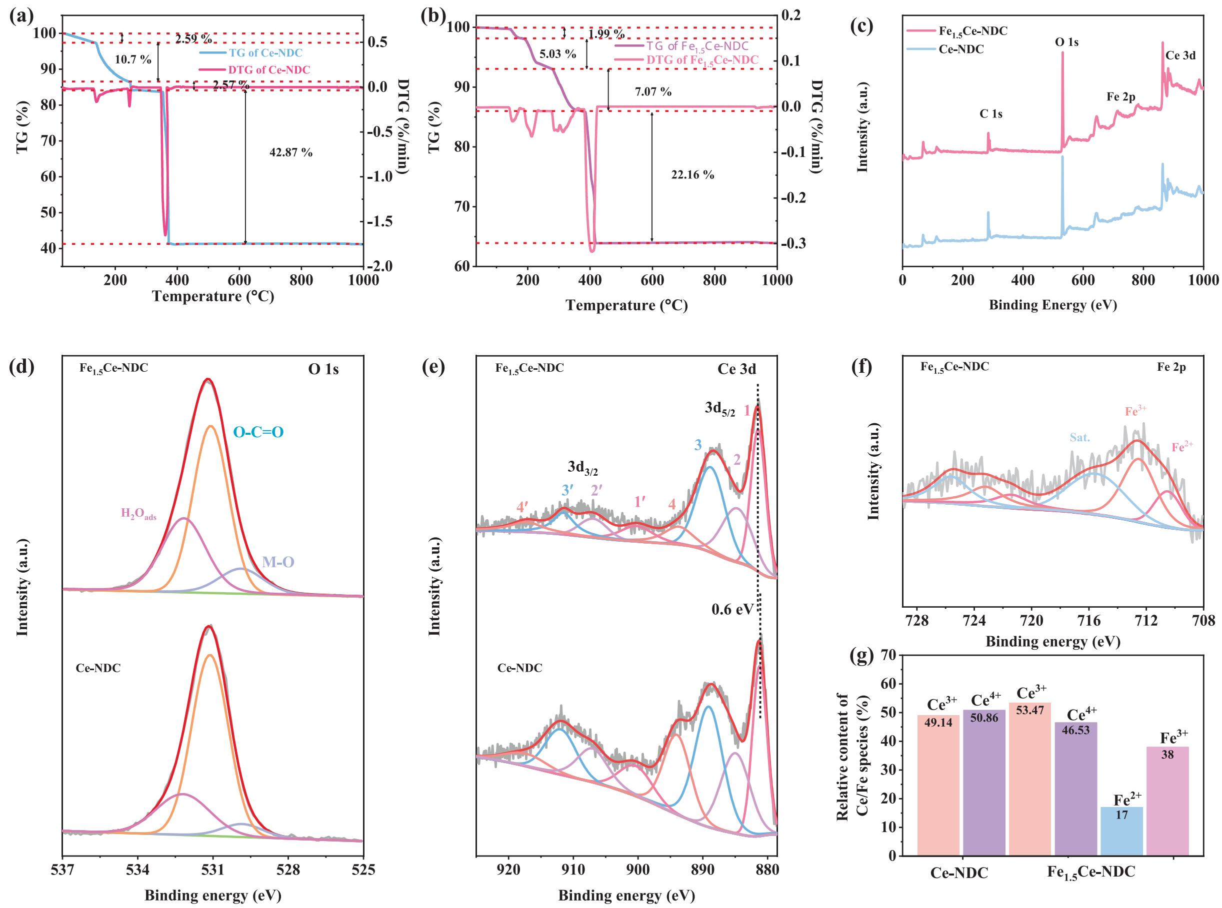

Fig. 3. TG/DTG curves of (a) Ce-NDC and (b) $Fe_{1.5}$Ce-NDC. (c) High-resolution XPS survey. (d) O 1 s, (e) Ce 3d, (f) Fe 2p, and (g) relative distribution of Ce and Fe species for Ce-NDC and $Fe_{1.5}$Ce-NDC.

attributed to the $3d_{5/2}$ region, while the peaks at 900.69 (1′), 907.12 (2′), 912.25 (3′), and 917.45 eV (4′) correspond to both Ce^{3+} and Ce^{4+} species, representing the typical features of the $3d_{3/2}$ region [34–36]. These observations demonstrate that both Ce^{3+} and Ce^{4+} are present in the Ce-NDC and $Fe_{1.5}$Ce-NDC, with the presence of Ce^{3+} being significant for the catalytic activity and electron transfer processes [37]. The minor shifts (0.6 eV) in peak positions for $Fe_{1.5}$Ce-NDC suggest that Fe incorporation slightly influences the electronic structure of Ce but does not drastically change the oxidation state distribution of Ce. Fe 2p XPS spectra of $Fe_{1.5}$Ce-NDC (Fig. 3f) illustrates peaks at 710.54 eV and 721.45 eV assigned to Fe^{2+} and 712.50 eV and 723.22 eV for Fe^{3+}, respectively, confirming the coexistence of both oxidation states. Satellite peaks at 715.77 eV and 725.50 eV is observed [38–40]. Relative contents of Ce^{3+}, Ce^{4+}, and Fe^{2+}, Fe^{3+} species in Ce-NDC and $Fe_{1.5}$Ce-NDC determined by XPS analysis (Fig. 3g). In Ce-NDC, Ce^{3+} and Ce^{4+} account for 49.14 % and 50.86 %, respectively, indicating an almost equal distribution of these oxidation states. However, Ce^{3+} increases to 53.47 % while Ce^{4+} decreases to 46.53 % in $Fe_{1.5}$Ce-NDC, suggesting that iron introduction favors a higher proportion of Ce^{3+}, thereby enhancing catalytic activity. Additionally, the presence of Fe^{2+} (17.10 %) and Fe^{3+} (38.19 %) in $Fe_{1.5}$Ce-NDC creates an efficient Fe^{2+}/ Fe^{3+} redox pair vital for electron transfer during OER.

3.2. OER electrocatalytic efficiency

OER electrocatalytic activity was assessed using a standard three-electrode configuration, including a reference, counter, and working electrode (Fig. 4a). All linear sweep voltammetry (LSV) measurements were adjusted with full (100 %) *iR* compensation. As illustrated in Fig. 4b, $Fe_{1.5}$Ce-NDC demonstrates the most effective electrocatalytic performance among all synthesized catalysts, achieving a low overpotential of 236 mV at 10 mA cm^{-2}. This value is significantly lower than those of Ce-NDC (316 mV), $Fe_{0.5}$Ce-NDC (303 mV), Fe_1Ce-NDC (293 mV), Fe_2Ce-NDC (250 mV), and also RuO_2 (265 mV). At elevated current densities, $Fe_{1.5}$Ce-NDC maintains superior activity, requiring only 281 mV at 50 mA cm^{-2} and 305 mV at 100 mA cm^{-2}, as shown in Fig. 4c, highlighting its outstanding electrocatalytic efficiency. $Fe_{1.5}$Ce-NDC exhibits excellent OER kinetics with a Tafel slope of 52 mV dec^{-1} (Fig. 4d), outperforming Ce-NDC (103 mV dec^{-1}), $Fe_{0.5}$Ce-NDC (88 mV dec^{-1}), Fe_1Ce-NDC (83 mV dec^{-1}), Fe_2Ce-NDC (59 mV dec^{-1}), and RuO_2 (69 mV dec^{-1}). This suggests that improved OER kinetics of $Fe_{1.5}$Ce-NDC. Notably, the electrochemical performance of $Fe_{1.5}$Ce-NDC surpasses that of previously documented OER electrocatalysts, as shown in Fig. 4e and **Table S1**. To better understand the enhanced OER activity, cyclic voltammetry (CV) measurement was carried out in the non-Faradaic region at several scan rates to calculate the electric double-layer capacitance (C_{dl}) (**Figs. S5a-e**), facilitating for a more detailed investigation of the ECSA. $Fe_{1.5}$Ce-NDC showed a C_{dl} value of 3.9 mF cm^{-2}, surpasses Ce-NDC 1.7 mF cm^{-2} (Fig. 4f), indicating its enhanced electric double-layer capacitance. Additionally, the $Fe_{1.5}$Ce-NDC exhibited an ECSA of 97 cm^2 (Fig. 4g), highlighting the increased exposure of active sites due to its unique porous structure. This enhanced surface area improved mass transfer efficiency and overall catalytic performance [41]. As shown in Fig. 4h, $Fe_{1.5}$Ce-NDC exhibited the lowest charge transfer resistance of 1.83 Ω, which highlights its superior electron transfer during the OER. In comparison, Ce-NDC, $Fe_{0.5}$Ce-NDC, Fe_1Ce-NDC, Fe_2Ce-NDC and RuO_2 showed charge transfer resistances of 2.49 Ω, 9.48 Ω, 14.32 Ω, 17.53 Ω, and 3.75 Ω,

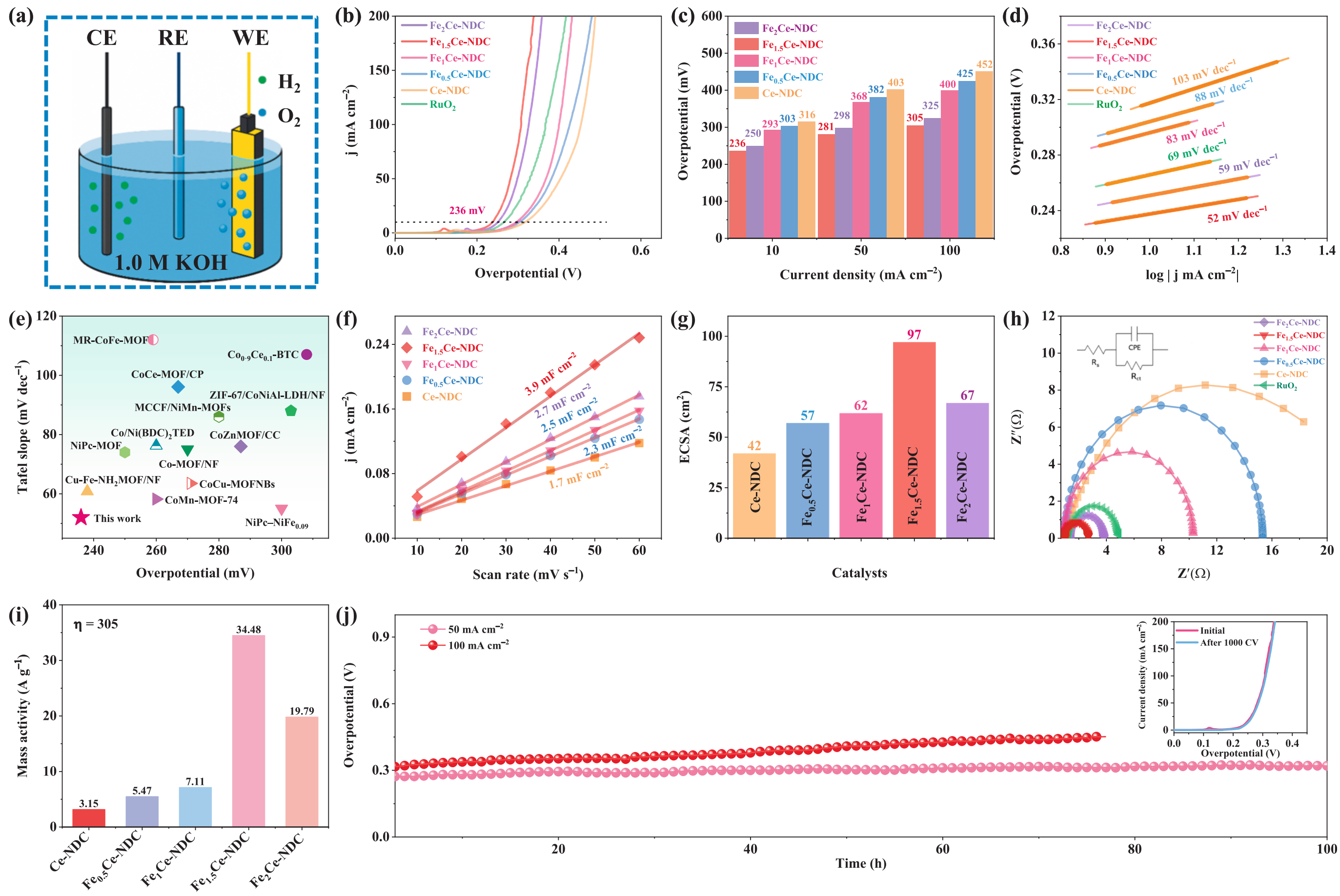

Fig. 4. OER performance in 1.0 M KOH solution. (a) A schematic of an electrochemical cell with distinct electrodes (CE, RE, WE) and gas evolution (O_2 and H_2). (b) LSV polarization curves. (c) Comparison of overpotential at various mA cm^{-2}. (d) Tafel slopes. (e) Overpotential and Tafel slope comparison with literature. (f) C_{dl} plots. (g) ECSA comparison. (h) Electrochemical impedance spectroscopy of prepared catalysts. (i) The mass activity values at overpotential of 305 mV. (j) Long-term durability test at 50 mA cm^{-2} and 100 mA cm^{-2} (inset: polarization curves before and after 1000 CV cycles).

respectively. These values underscore the efficient electron transfer capabilities of $Fe_{1.5}$Ce-NDC [42–44]. The corresponding equivalent circuit diagram, which complements the electrochemical data, is shown in the inset of Fig. 4h. Incorporation of Fe into the Ce-NDC structure enhanced electrical conductivity, leading to improved catalytic performance [45]. The mass catalytic activity of the different catalysts was calculated based on the current density values at a specific overpotential ($\eta = 305$ mV). As shown in the Fig. 4i, $Fe_{1.5}$Ce-NDC exhibited the highest mass activity of 34.48 A g^{-1}, followed by Fe_2Ce-NDC with 19.79 A g^{-1}, Fe_1Ce-NDC with 7.11 A g^{-1}, $Fe_{0.5}$Ce-NDC with 5.47 A g^{-1}, and Ce-NDC with 3.15 A g^{-1} [46]. These values indicate the superior catalytic performance of $Fe_{1.5}$Ce-NDC in comparison to other materials, underscoring its enhanced electron transfer capabilities. For real-world applications, long-term stability is essential for the effective performance of electrocatalysts. To assess the stability of $Fe_{1.5}$Ce-NDC, polarization curves were recorded as well as showed negligible changes after 1000 CV cycles **(inset,** Fig. 4j), highlighting its superior cycling stability. Moreover, the catalyst sustained a steady performance at 50 mA cm^{-2} for 100 h and 100 mA cm^{-2} for 76 h with negligeable activity loss (Fig. 4j), affirming its excellent long-term durability.

3.3. Operando electrochemical and spectroscopic insights into the OER mechanism

The electrochemical redox reaction of the active metal species in the system determines the structural evolution of catalysts during OER. This transformation creates highly active sites, which are crucial for enhancing OER efficiency. *In-situ* electrochemical impedance spectroscopy (EIS) was conducted to monitor the evolution of the catalysts and assess charge transfer behavior at the catalytic interface, thereby gaining deeper insights into these dynamic changes [47–49]. As the applied potential increases, the phase angle undergoes a noticeable shift (Figs. **5a-b)**, indicating enhanced reaction kinetics and improved adsorption of reactants. $Fe_{1.5}$Ce-NDC exhibits a significant reduction in phase angle across the applied potential range compared to Ce-NDC, suggesting that Fe incorporation facilitates a more efficient charge transfer process and promotes surface activation [12,50]. Notably, the complete transition for $Fe_{1.5}$Ce-NDC occurs at 1.45 V, whereas Ce-NDC undergoes this transition at a slightly higher potential of 1.55 V, further highlighting the improved electrocatalytic kinetics of $Fe_{1.5}$Ce-NDC [51,52]. Additionally, the EIS-derived Bode plots (Fig. 5**c)** provide further insights into the interfacial behavior, revealing phase angle variations at different applied potentials. The peaks in the low-frequency region (10^{-2}–10^{1} Hz) are associated with the OER process [34]. As depicted in **Figs. S6a-b**, the consistently lower phase angles of $Fe_{1.5}$Ce-NDC relative to Ce-NDC indicate that Fe incorporation enhanced electron transfer efficiency. This enhanced charge transport expedites reaction kinetics and significantly elevates the OER performance. Collectively, these results elucidate the critical role of Fe incorporation in Ce-NDC, enabling superior catalytic activity through enhanced charge transfer dynamics and structural stability.

To explore the electrochemical redox transition of Fe^{2+}/Fe^{3+} during OER, *operando* Raman was performed across a range of potentials, from the OCP up to 1.48 V. The *in-situ* Raman spectrum reveal a progressive

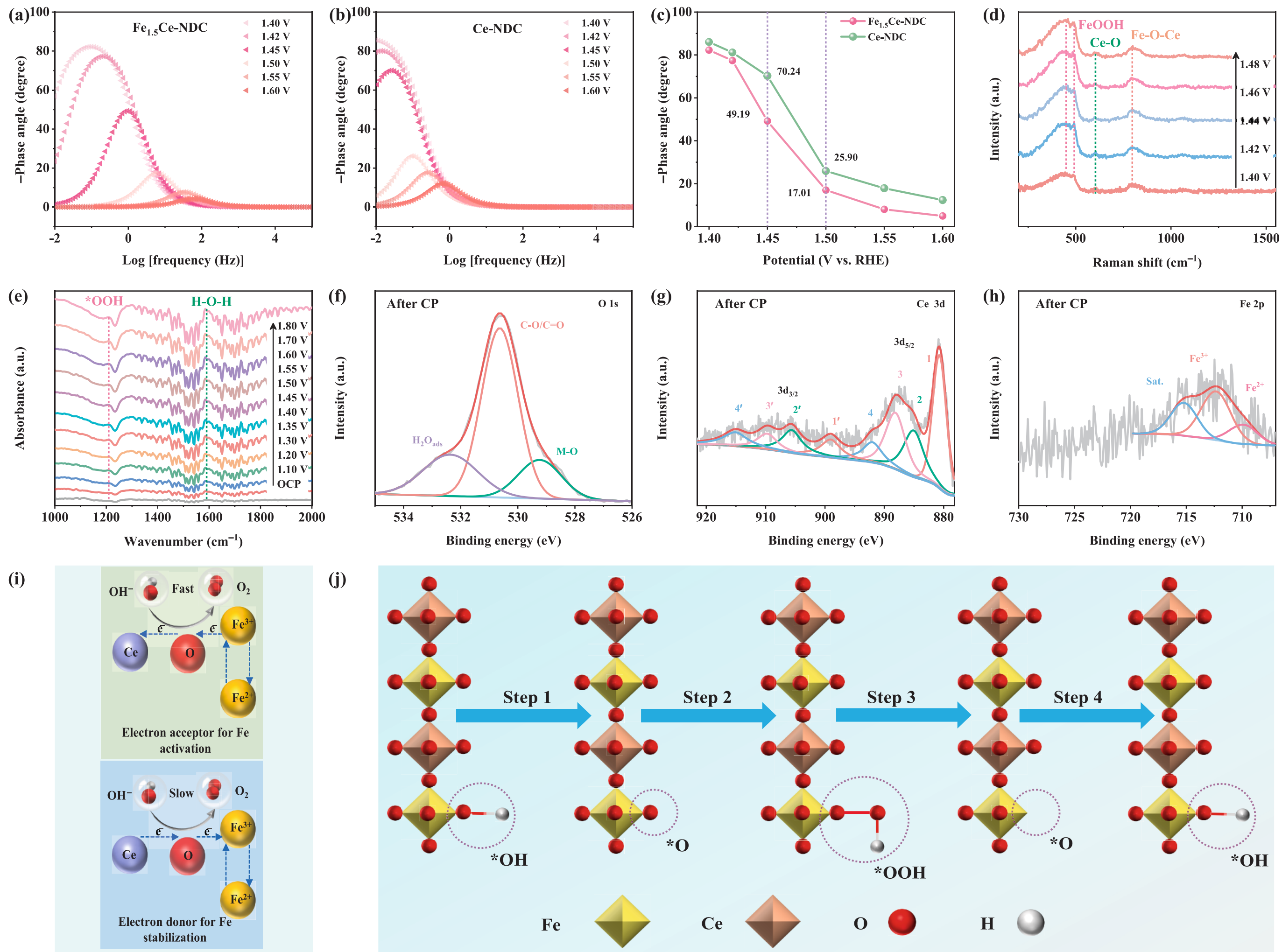

Fig. 5. *Operando* electrochemical and spectroscopic analysis. (a) Bode plots of $Fe_{1.5}$Ce-NDC and (b) Ce-NDC different applied potentials (vs. RHE). (c) Phase angle response as a function of applied potential for $Fe_{1.5}$Ce-NDC and Ce-NDC. (d) *Operando* Raman spectra of $Fe_{1.5}$Ce-NDC at different applied potentials (vs. RHE). (e) ATR-FTIR spectra of $Fe_{1.5}$Ce-NDC at various applied potentials (vs. RHE). High-resolution XPS spectra of (f) O 1 s, (g) Ce 3d, and (h) Fe 2p of $Fe_{1.5}$Ce-NDC after stability test. (i) Schematic illustration of the electron transfer mechanism in $Fe_{1.5}$Ce-NDC during the OER process. (j) Stepwise AEM for $Fe_{1.5}$Ce-NDC during the OER process.

transformation of $Fe_{1.5}$Ce-NDC, accompanied by the formation of FeOOH, Ce-O, and Fe-O-Ce species as the potential is introduced (Fig. 5d). A broad peak in the 450–500 cm^{-1} range corresponds to the E_g bending and A_{1g} stretching modes of FeOOH, confirming the formation of an electrochemically active phase during OER [53,54]. Notably, the Ce-O vibration is observed at 604 cm^{-1} and Fe-O-Ce bonding appears at 785 cm^{-1}, further confirming the interaction between Fe and Ce during the OER process. These observations indicate that FeOOH is the dominant active species, while the presence of Ce is essential for stabilizing the structure and improving electron transfer.

To better understand the OER mechanism, it is essential to identify the intermediate species that form during the catalytic process. *Operando* attenuated total reflectance Fourier-transform infrared spectroscopy (ATR-FTIR) was employed to track the evolution of oxygen-containing species. This technique provides real-time experimental evidence of reaction intermediates, offering a clearer understanding of the catalytic pathway. As showed in Fig. 5e, the *in-situ* ATR-FTIR spectra highlight the emergence of key intermediates during the OER. No distinct absorption bands are detected at OCP, confirming the absence of active oxygen species on the catalyst surface. However, as the applied potential increases, characteristic vibrational peaks emerge, forming key intermediates involved in the OER pathway. As the potential increases within the OER region, distinct peaks appear at 1207 cm^{-1}, corresponding to the formation of *OOH species, a crucial intermediate in the AEM. Additionally, the H-O–H stretching vibration appears at 1596 cm^{-1} assigned to the interaction of H_2O molecules with the catalytic surface, playing a role in the reaction mechanism [55–59]. These spectral observations validate the AEM, where sequential formation of oxygen species (*OOH). The increasing intensity of these peaks with higher applied potentials indicates the progressive accumulation of reactive intermediates, confirming their active role in enhancing the OER activity of $Fe_{1.5}$Ce-NDC. This further supports the superior catalytic performance of $Fe_{1.5}$Ce-NDC, as it efficiently facilitates oxygen evolution by the stabilization and conversion of key reaction intermediates.

After completing the OER stability test, SEM and XPS analyses were conducted to investigate the morphology and surface chemical states of $Fe_{1.5}$Ce-NDC. As shown in Fig. S7, the SEM analysis indicated slight changes in the morphology of $Fe_{1.5}$Ce-NDC after the stability test. The compositional transformation of $Fe_{1.5}$Ce-NDC after the OER process was further validated (**Figs. S8-9**). The O 1 s XPS spectra shows a negative shift, accompanied by a significant increase in the M—O peak intensity, indicating notable modifications in the oxygen bonding environment (Fig. 5f) [60,61]. This shift suggests stronger M—O interactions and potential structural rearrangements within the Fe-O-Ce framework. The

Ce 3d XPS spectra show a negative shift attributed to the change in the Ce oxidation state and the interaction with Fe/O species (Fig. 5g), suggesting that the enhanced redox activity of Ce^{3+}/Ce^{4+} during the OER resulted in a redistribution of electron density. Similarly, Fe 2p XPS spectra reveals a noticeable reduction in Fe^{2+} area, accompanied by an increase in Fe^{3+} area, indicating the oxidation of Fe species to form FeOOH during the reaction (Fig. 5h). A slight negative shift in the Fe 2p peak was observed, suggesting changes in the electronic environment and possible changes in the metal–oxygen interactions [62,63]. These negative shifts in O 1 s, Ce 3d, and Fe 2p peaks suggest the formation of active catalytic sites such as FeOOH, crucial in boosting OER performance. This dynamic surface reconstruction highlights the synergistic interaction between Fe and Ce, contributing to enhanced catalytic activity. These findings collectively demonstrate that the $Fe_{1.5}$Ce-NDC catalyst undergoes dynamic surface reconstruction during OER, where FeOOH serves as the active site, stabilized by Fe-Ce interactions, leading to enhanced charge transfer and superior catalytic performance.

Furthermore, Fig. 5i illustrates the dual role of Ce in modulating Fe activity during the OER. In the fast activation stage, Ce initially acts as an electron acceptor to facilitate Fe activation, promoting Fe^{2+} oxidation to Fe^{3+}, as confirmed by *operando* Raman spectra with FeOOH formation. This rapid electron transfer is crucial for initiating the OER mechanism [64]. In contrast, during the slow stabilization stage, Ce acts as an electron donor, helping to maintain Fe^{3+} oxidation states and preventing deactivation, ensuring prolonged catalytic efficiency, as evidenced by ATR-FTIR spectra showing OOH (1207 cm^{-1}) intermediate [65]. The presence of Ce-O (604 cm^{-1}) and Fe-O-Ce (785 cm^{-1}) bonds in *operando* Raman, further highlights the synergistic Fe-Ce interaction, enhancing charge transfer and active site stability. The AEM governing the OER on the $Fe_{1.5}$Ce-NDC catalyst proceeds through a four-step pathway (Fig. 5j), as confirmed by *operando* Raman and ATR-FTIR. In Step 1, hydroxide (*OH) ions from the electrolyte adsorb onto the active metal sites, initiating the reaction. This adsorption step is crucial for the subsequent oxidation process. In Step 2, the *OH species undergo deprotonation, forming *O intermediates. This step facilitates the oxidation of metal centers, allowing for the activation of oxygen species. In Step 3, an additional hydroxide ion interacts with the *O species, forming an *OOH intermediate. This intermediate is highly reactive and plays a key role in oxygen evolution. Finally, in Step 4, the *OOH species further deprotonate, releasing molecular oxygen (O_2) and regenerating the catalytic site for the next reaction cycle [14,66–68].

3.4. Overall water splitting

To assess the overall water-splitting performance, a two-electrode system was set up with $Fe_{1.5}$Ce-NDC as the anode and commercial Pt/C as the cathode (Fig. 6a). A reference electrolyzer was constructed using Pt/C as the cathode and RuO_2 as the anode ($Pt/C^{(-)}$ || $RuO_2^{(+)}$) for performance comparison. As shown in the LSV curve (Fig. 6b), the $Fe_{1.5}$Ce-$NDC^{(+)}$ || $Pt/C^{(-)}$ exhibited a lower operating voltage of 1.51 V at 10 mA cm^{-2}, surpassing the performance of the $RuO_2^{(+)}$ || $Pt/C^{(-)}$ system. The $Fe_{1.5}$Ce-$NDC^{(+)}$ || $Pt/C^{(-)}$ required lower voltages to achieve higher current densities, requiring only 1.65, 1.96, and 2.24 V to reach 100, 500, and 1000 mA cm^{-2}, respectively, confirming its superior catalytic efficiency (Fig. 6c). As shown in Fig. 6d and **Table S2**, the $Fe_{1.5}$Ce-$NDC^{(+)}$ || $Pt/C^{(-)}$ delivers exceptional performance at high current densities, highlighting its competitive edge among previously reported noble metal-free electrocatalysts. Moreover, the water electrolyzer exhibits robust long-term stability, operating at 50 and 100 mA cm^{-2} for 100 h without significant degradation (Fig. 6e).

In comparison to other studies on CoFe-MOFs used as OER catalysts, our work presents several key innovations in both material design and performance. While CoFe-MOFs have demonstrated promising catalytic activity in the past, the $Fe_{1.5}$Ce-NDC catalyst developed in this study stands out due to its unique combination of hierarchical porosity, synergistic Fe-Ce interactions, and dynamic surface reconstruction, which significantly enhance its catalytic performance and stability. Specifically, Ce which facilitates the stabilization of active Fe sites and optimizes the electronic structure, leading to a lower overpotential (236 mV) and exceptionally low Tafel slope (52 mV dec^{-1}) compared to

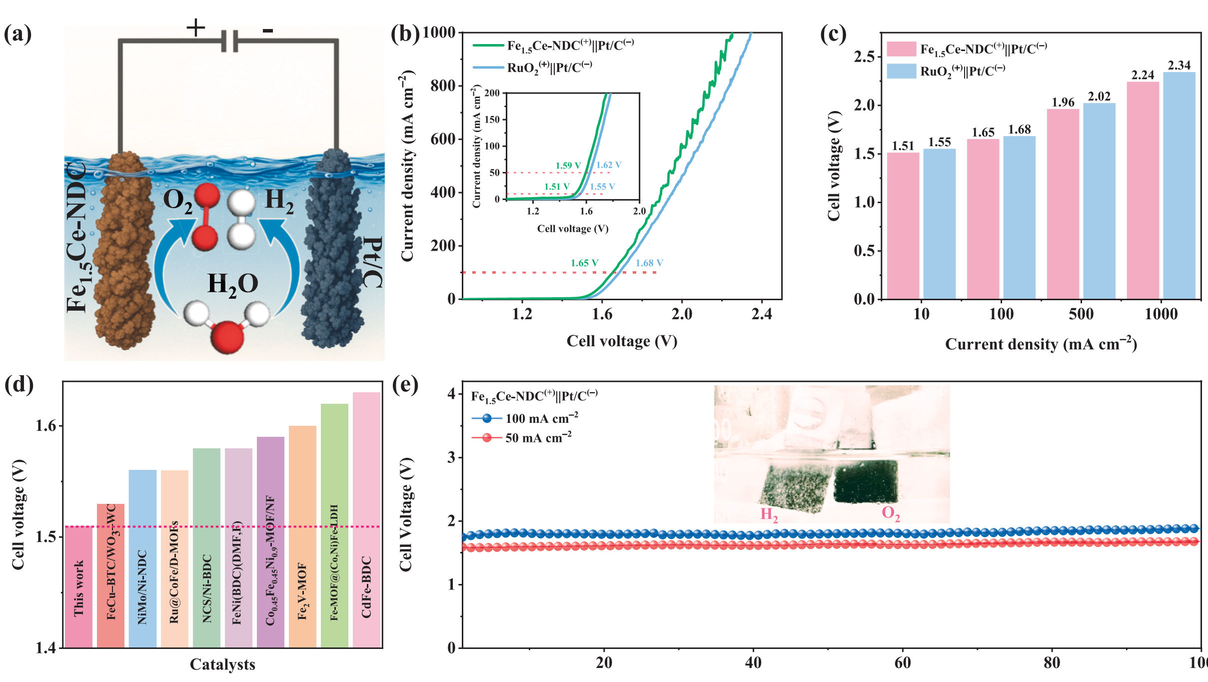

Fig. 6. Overall water-splitting performance of $Fe_{1.5}$Ce-NDC. (a) Schematic representation of the overall water-splitting process in a two-electrode system. (b) Polarization curves of $Fe_{1.5}$Ce-NDC $^{(+)}$ || Pt/C $^{(-)}$ with the reference $RuO_2^{(+)}$ || $Pt/C^{(-)}$. (c) Comparison of cell voltages required at varying current densities for $Fe_{1.5}$Ce-$NDC^{(+)}$ || $Pt/C^{(-)}$ and $RuO_2^{(+)}$ || $Pt/C^{(-)}$ systems. (d) Comparative analysis of the cell voltages of $Fe_{1.5}$Ce-NDC electrolyzers with previously reported water-splitting catalysts. (e) Long-term stability assessment utilizing CP at 50 and 100 mA cm^{-2} for 100 h (inset: experimental setup during the stability test).

traditional CoFe-MOFs and RuO_2 catalysts. Moreover, the long-term stability demonstrated by $Fe_{1.5}$Ce-NDC, which maintains performance over 76 h at high current densities, is a notable advancement over other CoFe-MOF-based catalysts, which often suffer from rapid degradation under prolonged operation [69–71]. The use of *operando* Raman and ATR-FTIR spectroscopy to confirm the AEM mechanism further differentiates this study, providing deeper insight into the catalytic mechanism and stability of the material. Therefore, $Fe_{1.5}$Ce-NDC catalyst not only offers enhanced OER performance and stability, but also presents a novel approach to optimizing the structure and dynamics of Fe-based MOFs for sustainable energy applications, distinguishing it from other CoFe-MOF-based electrocatalysts in the literature [72–74].

3.5. Key factors contributing to the superior OER performance

The outstanding OER catalytic activity, stability, and overall water-splitting performance of the $Fe_{1.5}$Ce-NDC are ascribed to following crucial characteristics. (1) The hierarchically porous nanostructures maximize active site exposure, enhance electrolyte diffusion, and boost oxygen evolution efficiency, thereby elevating the catalytic performance. (2) The synergistic interaction between Fe and Ce significantly improves charge transfer efficiency, as evidenced by *operando* EIS measurements, where $Fe_{1.5}$Ce-NDC exhibits a lower charge transfer resistance than Ce-NDC. (3) *Operando* Raman and ATR-FTIR confirm surface reconstruction, showing Fe transforms into active FeOOH sites vital for oxygen intermediate adsorption during OER. (4) XPS reveals a negative shift in Fe 2p binding energies, Fe^{2+} oxidation to Fe^{3+} and FeOOH formation. Simultaneously, the Ce^{3+}/Ce^{4+} transition enhances structural stability and electron transport. (5) Strong Fe-Ce interactions reduce oxygen intermediate adsorption energies and activation barriers, supporting an efficient OER pathway (*operando* spectroscopy). (6) $Fe_{1.5}$Ce-NDC also shows excellent stability, operating over 76 h at 100 mA cm^{-2} with no significant degradation, confirming its robustness for alkaline water-splitting. These combined features, efficient charge transfer, robust stability, active site exposure, and strong Fe-Ce synergy make $Fe_{1.5}$Ce-NDC an exceptional catalyst for both OER and electrolytic hydrogen production, positioning it as a promising candidate for renewable energy applications.

4. Conclusion

In conclusion, the $Fe_{1.5}$Ce-NDC electrocatalyst exhibits outstanding OER activity, with a low overpotential and Tafel slope, surpassing conventional RuO_2. The catalysts remarkable stability over 76 h at 100 mA cm^{-2} underscores its potential for long-term energy applications. The synergistic Fe-Ce interaction plays a critical role in enhancing charge transfer, promoting dynamic surface reconstruction, and stabilizing active sites. *Operando* Raman and ATR-FTIR spectroscopy confirm the formation of FeOOH as the active species, with Ce facilitating both the activation and stabilization of Fe. These findings highlight the importance of Fe-Ce interactions in optimizing the catalytic properties of MOFs, establishing $Fe_{1.5}$Ce-NDC as a promising candidate for effective and sustainable OER water splitting and other energy conversion processes.

CRediT authorship contribution statement

Sheraz Muhammad: Writing – original draft, Methodology, Investigation, Data curation. **Lixia Wang:** Writing – review & editing. **Mingcheng Gao:** Investigation. **Sumayya Khan:** Conceptualization. **Wentao Xu:** Data curation. **Asif Ali:** Methodology. **Tayirjan Taylor Isimjan:** Writing – review & editing. **Shohreh Azizi:** Writing – review & editing. **Xiulin Yang:** Writing – review & editing, Supervision.

Declaration of competing interest

The authors declare that they have no known competing financial interests or personal relationships that could have appeared to influence the work reported in this paper.

Acknowledgements

This work has been supported by the National Natural Science Foundation of China (no. 52363028, 21965005), Natural Science Foundation of Guangxi Province (2021GXNSFAA076001, 2018GXNSFAA294077), Guangxi Technology Base and Talent Subject (GUIKE AD23023004, GUIKE AD20297039).

Appendix A. Supplementary data

Supplementary data to this article can be found online at https://doi.org/10.1016/j.fuel.2025.136782.

Data availability

Data will be made available on request.

References

[1] Feng C, An Q, Zhang Q, Huang L, Wang N, Zhang X, et al. Unleashing the potential of Ru/FeCo-MOF in water splitting and supercapacitors through Morphology and electronic structure control. Int J Hydrogen Energy 2024;55:189–98.
[2] Li Y, Feng A, Dai L, Xi B, An X, Xiong S, et al. Progress on the design of electrocatalysts for large-current hydrogen production by tuning thermodynamic and kinetic factors. Adv Funct Mater 2024;34(28):2316296.
[3] Qin H, Cheng J, Zhou P, Ji Z, Peng H, Shen X, et al. In situ semi-etching of bimetallic LDH nanosheet arrays into FeNi-LDH/MOF to boost oxygen evolution reaction. Chem Eng J 2024;493:152721.
[4] Muhammad S, Wang L, Huang Z, Zhou A, Bilal H, Taylor Isimjan T, et al. Recent advances in lanthanide-based materials for oxygen evolution reaction: challenges and future prospects. Coord Chem Rev 2025;534:216573.
[5] Li S, Tang D, Jing X. Metal-organic framework-based self-supported electrodes for oxygen evolution reaction. Chem Synth 2024;4(4):70.
[6] Adegoke KA, Oyebamiji AK, Adeola AO, Olabintan AB, Oyedotun KO, Mamba BB, et al. Iron-based metal–organic frameworks and derivatives for electrochemical energy storage and conversion. Coord Chem Rev 2024;517:215959.
[7] Li C, Zhang H, Liu M, Lang F-F, Pang J, Bu X-H. Recent progress in metal–organic frameworks (MOFs) for electrocatalysis. Ind Chem Mater 2023;1(1):9–38.
[8] Song K, Feng X, Zhang N, Ma D, Shi L, Chen Y, et al. Metal-organic framework materials in NH_3-SCR: progress and prospects. Coord Chem Rev 2025;535:216615.
[9] Morelli Venturi D, Sole Notari M, Trovarelli L, Mosconi E, Alothman AA, Molokova A, et al. Synthesis, structure and (Photo)catalytic behavior of Ce-MOFs containing perfluoroalkylcarboxylate linkers: experimental and theoretical insights. Chem Eur J 2024;30(31):e202400433.
[10] Dai Y, Yu J, Zhang Z, Cheng C, Tan P, Shao Z, et al. Interfacial La diffusion in the $CeO_2/LaFeO_3$ hybrid for enhanced oxygen evolution activity. ACS Appl Mater Interfaces 2021;13(2):2799–806.
[11] Ai L, Luo Y, Huang W, Tian Y, Jiang J. Cobalt/cerium-based metal-organic framework composites for enhanced oxygen evolution electrocatalysis. Int J Hydrogen Energy 2022;47(26):12893–902.
[12] Wei X, Yu S, Li J, Liu T, Li S, Hata S, et al. Ce-doped nanorod-like NiFe-MOF with coordination substitution based on in situ co-doping method for boosting the oxygen evolution reaction. J Mater Chem A 2024;12(43):29886–97.
[13] Liao Y, Xiao Y, Li Z, Zhou X, Liu J, Guo F, et al. Structural engineering of Co-metal–organic frameworks via Ce incorporation for improved oxygen evolution. Small 2024;20(12):2307685.
[14] Zhao X, Yang Y, Liu Y, Shi J, Li Q, Xu Q, et al. Ultrathin Ni–Fe MOF nanosheets: efficient and durable water oxidation at high current densities. Langmuir 2024;40(25):13122–33.
[15] Dai S, Liu Y, Mei Y, Hu J, Wang K, Li Y, et al. Iron-doped novel Co-based metal–organic frameworks for preparation of bifunctional catalysts with an amorphous structure for OER/HER in alkaline solution. Dalton Trans 2022;51(40):15446–57.
[16] Das SK, Chatterjee S, Bhunia S, Mondal A, Mitra P, Kumari V, et al. A new strongly paramagnetic cerium-containing microporous MOF for CO_2 fixation under ambient conditions. Dalton Trans 2017;46(40):13783–92.
[17] Liu Y-H, Chien P-H. A series of lanthanide–organic frameworks possessing arrays of 2D intersecting channels within a 3D pillar-supported packed double-decker network and Co^{2+}-induced luminescence modulation. CrstEngComm 2014;16(37):8852–62.

[18] Rogowska M, Hansen P-A, Sønsteby HH, Dziadkowiec J, Valen H, Nilsen O. Molecular layer deposition of photoactive metal-naphthalene hybrid thin films. Dalton Trans 2021;50(37):12896–905.
[19] Mi S, Chen L, Zhang X, Zhang Q, Ma L, Liu J. Selective hydrogenation of vanillin over a graphene-encapsulated nitrogen-doped bimetallic magnetic Ni/Fe@NDC nano-catalyst. RSC Adv 2024;14(24):16747–57.
[20] Zhang X, Wang D, Nagaumi H, Wu Z, Zhang M, Wang R, et al. Unveiling the growth mechanism of Fe-containing intermetallics in Al–Si alloy in the perspective of surface stability and atom adsorption. J Mater Res Technol 2025;35:2458–70.
[21] Li X, Liu P, Wang Z, Liu P, Wei X, Wu Y, et al. Catalytic cracking of biomass tar for hydrogen-rich gas production: parameter optimization using response surface methodology combined with deterministic finite automaton. Renew Energy 2025; 241:122368.
[22] Huang Z, Liao M, Zhang S, Wang L, Gao M, Luo Z, et al. Valence electronic engineering of superhydrophilic Dy-evoked Ni-MOF outperforming RuO_2 for highly efficient electrocatalytic oxygen evolution. J Energy Chem 2024;90:244–52.
[23] Liu L, Zhang D, Zhu Y, Han Y. Bulk and local structures of metal–organic frameworks unravelled by high-resolution electron microscopy. Commun Chem 2020;3(1):99.
[24] Zhan Z, Liu Y, Wang W, Du G, Cai S, Wang P. Atomic-level imaging of beam-sensitive COFs and MOFs by low-dose electron microscopy. Nanoscale Horiz 2024; 9(6):900–33.
[25] Wu Q, Siddique MS, Guo Y, Wu M, Yang Y, Yang H. Low-crystalline bimetallic metal-organic frameworks as an excellent platform for photo-Fenton degradation of organic contaminants: Intensified synergism between hetero-metal nodes. Appl Catal B Environ Energy 2021;286:119950.
[26] Wang X-Y, Wei W-J, Zhou S-Y, Pan Y-Z, Yang J, Gan T, et al. Phosphorus-doped single atom copper catalyst as a redox mediator in the cathodic reduction of quinazolinones. Angew Chem Int Ed 2025;64(22):e202505085.
[27] Yang C-J, Huang Y-D, Zhang Y-Y, Pan Y-Z, Yang J, Pan Y-M, et al. A Mn–Rh dual single-atom catalyst for inducing C–C cleavage: relay catalysis reversing chemoselectivity in C–H oxidation. Chem Sci 2025;16(17):7329–38.
[28] Gu J-X, Chen H, Ren Y, Gu Z-G, Li G, Xu W-J, et al. A Novel Cerium(IV)-based metal-organic framework for CO_2 chemical fixation and photocatalytic overall water splitting. ChemSusChem 2022;15(1):e202102368.
[29] Tan B, Wu Z-F, Huang X-Y. An iron-NDC framework with a cage structure and an optothermal conversion in NIR window. Molecules 2022;27(24):8789.
[30] Tahir M, Dai J, Nisa FU, Naseem M, Qu L, Ma Z, et al. Modulating intrinsic sulfate ions in FeOOH nanorods for enhanced energy storage and catalytic oxygen evolution. Small;21(12):2412645.
[31] Chalmpes N, Bourlinos AB, Alsmaeil AW, Aljarrah AS, Salmas CE, Karakassides MA, et al. First synthesis of 2D materials by hypergolic reactions and evaluation of their dispersions for ink formulation: hexagonal boron nitride and fluorinated carbon nanosheets. Mater Res Express 2024;11(3):035002.
[32] Zhang N, Wang B, Hu P, Gao Z, Wang H. Achieve high-efficiency photocatalytic hydrogen production of MCNTs-CdS/Pt/$ZnFe_2O_4$ heterojunction owing to building charge transport bridge. J Environ Chem Eng 2025;13(2):115800.
[33] Wang H, Lin X, Huang Y, Bian W, Ma L. Two advanced oxidation pathways of modified iron-shavings participation in ozonation. Sep Purif Technol 2020;244: 116838.
[34] Wei F, Shen J, Xie J, Luo Z, Shi L, Isimjan TT, et al. Dynamic in situ reconstruction of $NiSe_2$ promoted by interfacial $Ce_2(CO_3)_2O$ for enhanced water oxidation. J Energy Chem 2024;98:472–80.
[35] Hu M, Ji W, Wang L, Lv S, Zhao Q, Hao Y. Structure and electrical properties of Al_2O_3 doped Ca–Ce–Ti–W–O NTC ceramics at high temperature. J Mater Sci Mater Electron 2022;33(35):26157–66.
[36] Shi L, Zhu K, Yang Y, Liu Y, Xu S, Isimjan TT, et al. Oxygen-vacancy-rich Ru-clusters decorated Co/Ce oxides modifying ZIF-67 nanocubes as a high-efficient catalyst for $NaBH_4$ hydrolysis. Int J Hydrogen Energy 2022;47(89):37840–9.
[37] Li X, You S, Du J, Dai Y, Chen H, Cai Z, et al. ZIF-67-derived Co_3O_4@carbon protected by oxygen-buffering CeO_2 as an efficient catalyst for boosting oxygen reduction/evolution reactions. J Mater Chem A 2019;7(45):25853–64.
[38] Yin H, Huang M, Wang L, Muhammad S, Isimjan TT, Guo J, et al. Lattice-mismatched MOF-on-MOF nanosheets with rich oxygen vacancies show fast oxygen evolution kinetics for large-current water splitting. Appl Catal B Environ Energy 2025;367:125105.
[39] Xu C. Design and preparation of Ag/AgCl/NH_2-MIL-101 (Fe) ternary composite photocatalysts with visible light application prospects. IOP Conf Ser: Earth Environ Sci 615 IOP Publishing 2020. 012121.
[40] Lopez Luna M, Timoshenko J, Kordus D, Rettenmaier C, Chee SW, Hoffman AS, et al. Role of the oxide support on the structural and chemical evolution of Fe catalysts during the hydrogenation of CO_2. ACS Catal 2021;11(10):6175–85.
[41] Hupele M, Raj R, Rai S, Sen T, Kanta Haldar K. Insight into the Coupling of HgS and CuO with Metal-organic frameworks support in electrocatalytic oxygen evolution reaction. ChemPhysChem;26(4):e202400956.
[42] Zhang Q, Wang X, Jian T, Ma W, Xu C, Zhou Q, et al. Free-standing multiscale porous high entropy NiFeCoZn alloy as the highly active bifunctional electrocatalyst for alkaline water splitting. Chin J Chem 2024;42(13):1465–73.
[43] Zhou Q, Hao Q, Li Y, Yu J, Xu C, Liu H, et al. Free-standing trimodal porous NiZn intermetallic and Ni heterojunction as highly efficient hydrogen evolution electrocatalyst in the alkaline electrolyte. Nano Energy 2021;89:106402.
[44] Zhou Q, Xu C, Li Y, Xie X, Liu H, Yan S. Synergistic coupling of NiFeZn-OH nanosheet network arrays on a hierarchical porous NiZn/Ni heterostructure for highly efficient water splitting. Sci China Mater 2022;65(5):1207–16.
[45] Fu H, Lian Y, Hu Y, Zhao J, Zhang H. N-doping Fe-C@Nb_2CT_x MXenes with high stability and strong activity for sodium-ion storage and overall water splitting. Small 2025;21(7):2406131.
[46] Zhang L, Zhang N, Shang H, Sun Z, Wei Z, Wang J, et al. High-density asymmetric iron dual-atom sites for efficient and stable electrochemical water oxidation. Nat Commun 2024;15(1):9440.
[47] Huang Z, Bi Y, She J, Liu Y, Feng S, Xu C, et al. Vacancy-occupation triggered phase transformation in molybdenum disulfide with reduced energy barrier for enhanced alkaline water electrolysis. J Energy Chem 2025;106:619–30.
[48] Zhou Q, Xu C, Hou J, Ma W, Jian T, Yan S, et al. Duplex interpenetrating-phase FeNiZn and $FeNi_3$ heterostructure with low-gibbs free energy interface coupling for highly efficient overall water splitting. Nano-Micro Lett 2023;15(1):95.
[49] Pan Y, Gao J, Lv E, Li T, Xu H, Sun L, et al. Integration of alloy segregation and surface Co-O hybridization in carbon-encapsulated CoNiPt alloy catalyst for superior alkaline hydrogen evolution. Adv Funct Mater 2023;33(41):2303833.
[50] Jia J, Huang J, Guo K, Cha Y, Wang D, Tu M, et al. Ce-anchored NiFeOOH derived from in-situ self-optimization for efficient and highly durable water oxidation. Chem Eng J 2024;494:153195.
[51] Wu T, Xu S, Zhang Z, Luo M, Wang R, Tang Y, et al. Bimetal modulation stabilizing a metallic heterostructure for efficient overall water splitting at large current density. Adv Sci 2022;9(25):2202750.
[52] Yang Y, Lie WH, Unocic RR, Yuwono JA, Klingenhof M, Merzdorf T, et al. Defect-promoted Ni-based layer double hydroxides with enhanced deprotonation capability for efficient biomass electrooxidation. Adv Mater 2023;35(48):2305573.
[53] Liu H, Zhou X, Ye C, Ye M, Shen J. In-situ constructing oxide-anion dual-layer on Ce-B-containing electrode electrolyte interface towards highly corrosive seawater splitting. Appl Catal B Environ Energy 2024;343:123560.
[54] Zhao Y, Dongfang N, Triana CA, Huang C, Erni R, Wan W, et al. Dynamics and control of active sites in hierarchically nanostructured cobalt phosphide/ chalcogenide-based electrocatalysts for water splitting. Energy Environ Sci 2022; 15(2):727–39.
[55] Kumar G, Haldar R, Shanmugam M, Dey RS. Mechanistic insight into a Co-based metal–organic framework as an efficient oxygen electrocatalyst via an in situ FT-IR study. J Mater Chem A 2023;11(48):26508–18.
[56] Chang J, Shi Y, Wu H, Yu J, Jing W, Wang S, et al. Oxygen radical coupling on short-range ordered Ru atom arrays enables exceptional activity and stability for acidic water oxidation. J Am Chem Soc 2024;146(19):12958–68.
[57] Luo X, Zhao H, Tan X, Lin S, Yu K, Mu X, et al. Fe-S dually modulated adsorbate evolution and lattice oxygen compatible mechanism for water oxidation. Nat Commun 2024;15(1):8293.
[58] Liao D, Tian G, Xiaoyu F, Li Z, Sun Y, Chang W, et al. Toward an active site–performance relationship for oxide-supported single and few atoms. ACS Catal 2025;15(10):8219–29.
[59] Zhang L, Lei Y, Wang X, Lv E, Li J, Zhang N, et al. Synergistic long-range interaction of Co-Cu dual-atom sites on hollow CeO_2 nanostructures for bifunctional oxygen electrocatalysis. Adv. Funct. Mater.;35(31):e11730.
[60] Li W, Li F, Yang H, Wu X, Zhang P, Shan Y, et al. A bio-inspired coordination polymer as outstanding water oxidation catalyst via second coordination sphere engineering. Nat Commun 2019;10(1):5074.
[61] Li R, Hu B, Yu T, Chen H, Wang Y, Song S. Insights into correlation among surface-structure-activity of cobalt-derived pre-catalyst for oxygen evolution reaction. Adv Sci 2020;7(5):1902830.
[62] Chen X, Wang Q, Cheng Y, Xing H, Li J, Zhu X, et al. S-doping triggers redox reactivities of both iron and lattice oxygen in FeOOH for low-cost and high-performance water oxidation. Adv Funct Mater 2022;32(26):2112674.
[63] Zhang B, Shan J, Wang X, Hu Y, Li Y. Ru/Rh cation doping and oxygen-vacancy engineering of FeOOH nanoarrays@$Ti_3C_2T_x$ MXene heterojunction for highly efficient and stable electrocatalytic oxygen evolution. Small 2022;18(25):2200173.
[64] Mondal A, Velpandian M, Das HT, Sinhamahapatra A, Basu S, Afzal M. Fabrication of defective mesoporous cerium oxide nanostructure for promoting an efficient and stable electrocatalytic oxygen evolution reaction. Next Mater 2024;3:100169.
[65] Gao L, Yao Y, Chen Y, Huang J, Ma Y, Chen W, et al. Ce-4f as an electron-modulation reservoir weakening Fe-O bond to induce iron vacancies in CeFevNi hydroxide for enhancing oxygen evolution reaction. J Colloid Interface Sci 2024; 672:86–96.
[66] Mu X, Yu M, Liu X, Liao Y, Chen F, Pan H, et al. High-entropy ultrathin amorphous metal–organic framework-stabilized Ru(Mo) dual-atom sites for water oxidation. ACS Energy Lett 2024;9(12):5763–70.
[67] Liu T, Lu J, Chen Z, Luo Z, Ren Y, Zhuge X, et al. Advances, mechanisms and applications in oxygen evolution electrocatalysis of gold-driven. Chem Eng J 2024; 496:153719.
[68] Muhammad S, Yao B, Zhou A, Huang Z, Khan S, Wei F, et al. Unveiling dynamic surface transformations: Mo-doped Fe-based MOFs as next-generation oxygen evolution catalysts. Green Chem 2025;27(19):5554–66.
[69] Hou X, Zhou J, Xu X, Wang X, Zhang S, Wang H, et al. Morphological modulation of CoFe-based metal organic frameworks for oxygen evolution reaction. Catal Commun 2022;165:106445.
[70] Liang H, Lv Y, Tang K, Chai Y, Yang Y, Yang Z, et al. Enhanced oxygen evolution reaction catalytic properties of novel nanowire structures from FeCo-MOFs/GO via low-temperature annealing. Energy Technol 2024;12(10):2400058.
[71] Burud M, Patil SA, Jadhav V, Chougale P, Mane-Gavade S, Ustad R, et al. Synergistic effect of CoFe bimetallic MOF for efficient electrocatalytic OER in alkaline media. Energy Fuels 2025;39(28):13648–57.

[72] Liu Y, Li P, Wang Z, Gao L. Shape–preserved CoFeNi–MOF/NF exhibiting superior performance for overall water splitting across alkaline and neutral conditions. Materials 2024;17(10):2195.

[73] Kim DH, Moon J, Lee SY, An HJ, Jeong H, Park JT. Fe-modulated NH_2–CoFe MOF nanosheet arrays on nickel foam by cation exchange reaction for an efficient OER electrocatalyst at high current density in alkaline water/seawater. CrstEngComm 2023;25(38):5387–98.

[74] Deng S, Li Z, Xu K, Liu Z, Yin Z, Yu H, et al. Composition-balanced bi-metallic MOFs directly grown on nickel foam for high-efficiency oxygen evolution reaction. J Electrochem Soc 2021;168(8):082504.